

INTERNAL GRAVITY WAVES IN THE MAGNETIZED SOLAR ATMOSPHERE. I. MAGNETIC FIELD EFFECTS

G. VIGEESH^{1,2}, J. JACKIEWICZ², AND O. STEINER^{1,3}

¹Kiepenheuer-Institut für Sonnenphysik, Schöneckstrasse 6, 79104 Freiburg, Germany

²New Mexico State University, Department of Astronomy, P.O. Box 30001, MSC 4500, Las Cruces, NM 88003, USA
and

³Istituto Ricerche Solari Locarno (IRSOL), via Patocchi 57–Prato Pernice, 6605 Locarno-Monti, Switzerland

ABSTRACT

Observations of the solar atmosphere show that internal gravity waves are generated by overshooting convection, but are suppressed at locations of magnetic flux, which is thought to be the result of mode conversion into magneto-acoustic waves. Here, we present a study of the acoustic-gravity wave spectrum emerging from a realistic, self-consistent simulation of solar (magneto-)convection. A magnetic field free, hydrodynamic simulation and a magneto-hydrodynamic (MHD) simulation with an initial, vertical, homogeneous field of 50 G flux density were carried out and compared with each other to highlight the effect of magnetic fields on the internal gravity wave propagation in the Sun’s atmosphere. We find that the internal gravity waves are absent or partially reflected back into the lower layers in the presence of magnetic fields and argue that the suppression is due to the coupling of internal gravity waves to slow magneto acoustic waves still within the high- β region of the upper photosphere. The conversion to Alfvén waves is highly unlikely in our model because there is no strongly inclined magnetic field present. We argue that the suppression of internal waves observed within magnetic flux-concentrations may also be due to non-linear breaking of internal waves due to vortex flows that are ubiquitously present in the upper photosphere and the chromosphere.

Keywords: magnetohydrodynamics (MHD) — Sun: atmosphere — Sun: granulation — Sun: magnetic fields — Sun: photosphere — waves

1. INTRODUCTION

The solar atmosphere provides a favourable environment for the generation and propagation of internal gravity waves (or internal waves). Turbulent convection from subsurface regions penetrating locally into a stably stratified medium above it, is thought to excite internal waves, along with acoustic waves. These waves couple the lower atmosphere with the higher layers by transporting energy, and presumably contributing to the heating of the upper solar atmosphere. However, the short radiative timescales and the presence of strong magnetic fields in these regions influence the internal waves. The effects that magnetic fields may have on the generation and propagation of these waves are still unknown.

Internal waves are a natural response of a gravitationally stratified medium to any disturbance of its equi-

librium state, with buoyancy acting as the equilibrium restoring force. Internal waves are ubiquitous in the Earth’s atmosphere and have been extensively studied for their role in the circulation patterns in the oceans and the terrestrial atmosphere. They form an essential component in the general circulation models (GCM) that provide accurate global weather predictions. The downward propagating, east-west oscillatory patterns known as Quasi-Biennial Oscillations (QBO) observed in the Earth’s atmosphere below 35 km in tropical latitudes are due to momentum transport by internal waves. Tsunamis in open oceans excite internal waves that propagate up to ionospheric heights causing traveling ionospheric disturbances (Artru et al. 2005).

Studies of internal waves in the solar atmosphere began with Whitaker (1963) following a suggestion by Hines (1960), a pioneer in the field of terrestrial atmospheric physics, that internal waves could play an important role in coronal heating. Later work invoked internal waves to explain the then elusive 5-min oscillations

of the solar atmosphere (Leighton 1960; Leighton et al. 1962). The theoretical framework put forth by Moore & Spiegel (1964) tried to explain these oscillations due to frequencies below the acoustic cut-off value, a regime where the internal gravity waves exist. Later, a number of works explored the existence of trapped internal gravity waves due to a temperature dip (Uchida 1965, 1967) or due to ionization effects (Thomas et al. 1971) and related those to the observed solar oscillations. These studies later gave way to trapped acoustic waves in the solar interior as the sole agent responsible for the oscillations (Ulrich 1970; Leibacher & Stein 1971). Despite the fact that they did not play a role in the observed oscillations, studies of internal waves continued in view of explaining the heating of the upper atmosphere.

Lighthill (1967) suggested that internal waves are efficiently generated by “tongues of turbulence” that reach up into the photosphere where they contribute to atmospheric heating. Stein (1967) discussed the generation of internal waves by turbulence in an isothermal, stratified atmosphere. However, the short radiative relaxation times in the photosphere raised questions about the mere existence of internal waves in these regions (Schatzman & Souffrin 1967; Kuperus 1969; Stix 1970; Clark & Clark 1973; Logan & Hill 1980). Analytical studies of the complete magneto-acoustic-gravity (MAG) spectrum in a simple stratified atmosphere have been carried out by a number of authors starting with Ferraro & Plumpton (1958), Zhugzhda & Dzhililov (1982), Leroy & Schwartz (1982), Zhugzhda & Dzhililov (1984), Hasan & Christensen-Dalsgaard (1992), Bogdan & Cally (1997), Cally (2001), Campos & Marta (2015), to cite a few.

Some of the first observational evidences suggesting the existence of internal waves in the solar atmosphere were presented by Schmieder (1976) and Cram (1978). An extensive study of internal waves in the solar atmosphere focusing on the energy dissipation and their possible signatures on spectral lines was carried out by Mihalas & Toomre (1981, 1982). They concluded that the energy dissipation of internal waves due to non-linear wave-breaking is dominant in the mid-chromosphere and that they deposit all of their energy at these heights, hardly ever reaching the corona. While the detection of internal waves in the solar atmosphere has been questioned (Frazier 1968; Lites & Chipman 1979), a series of observations reported evidence of internal waves in the solar atmosphere (Durrant & Nesis 1981; Staiger et al. 1984; Staiger 1987; Deubner & Fleck 1989; Marmolino & Severino 1991; Bonet et al. 1991; Komm et al. 1991; Kneer & von Uexküll 1993; Straus & Bonaccini 1997; Krijger et al. 2001; Rutten & Krijger 2003).

Using high spatial and temporal resolution spectroscopic observations in multiple lines with ground and

space-based telescopes and with the help of 3D numerical simulation, Straus et al. (2008) reported the first “unambiguous” detection of propagating internal waves in a magnetically quiet region of the solar atmosphere. They claimed that the energy flux of internal waves was sufficient for balancing the radiative losses of the chromosphere. They also observed that internal waves are suppressed in strong magnetic field regions as a result of reflection and conversion to other wave modes. Soon after, Stodilka (2008) found signatures of internal waves in temperature fluctuations derived from the Fe I ($\lambda=532.418$ nm) spectral line, a temperature sensitive line formed at photospheric heights, raising questions about their presence at these heights despite strong radiative damping. Kneer & Bello González (2011) have reported the presence of internal waves and estimated their energy flux using observations in the lines of Fe I ($\lambda=557.6$ nm, 543.4 nm) that form at an average height of 380 km and 570 km, respectively. Recent work by Nagashima et al. (2014) also shows signature of internal waves in the SDO/HMI Dopplergrams. However, the numerical models in their work fail to show a clear signature of internal waves. This discrepancy may be due to the extent of the simulated domain, or the radiative damping in the model, or the upper boundary conditions. Despite recent observational confirmation of the existence of internal waves in the solar atmosphere, not much research was done towards understanding the power suppression of these waves in magnetic field regions.

Many different wave co-exist and interact with each other in the solar atmosphere. The surface-gravity waves (f -mode) and the evanescent tails of the solar p -modes exist in the atmosphere. In magnetic flux tubes, magneto-acoustic waves are generated as a result of continuous buffeting by granules (Hasan & Kalkofen 1999) and by strong inter-granular downdrafts (Kato et al. 2011), which propagate upwards and partially escape the flux tube to propagate as acoustic waves in the medium outside (Vigeesh et al. 2009). The magneto-acoustic waves that propagate up along the flux tubes undergo transmission and conversion at the equipartition level, the height where the ratio of sound speed (c_S) to Alfvén speed (v_A) drops below 1. The resulting fast magneto-acoustic waves get partially refracted travelling downwards in the atmosphere and partially convert to Alfvén waves near the apex of the refractive wave path (Khomenko & Cally 2012). Internal waves can also couple to magneto-acoustic and Alfvén waves as shown by Newington & Cally (2010, 2011). The whole sequence of wave production and coupling, starting from the solar surface up to heights where Alfvén waves are produced, has to be clearly understood in order to account for the energy distribution among various wave modes at differ-

ent heights. Radiative damping in the low-photosphere and non-linear effects leading to wave-breaking above the mid-chromosphere, spatially restrict the propagation of internal waves in the Sun’s atmosphere, making their observation difficult.

In this paper, we use realistic numerical simulations of the solar atmosphere to study the acoustic-gravity wave spectrum’s properties in the presence of magnetic fields. This work is a substantial extension to the linear analysis that was carried out by [Mihalas & Toomre \(1981, 1982\)](#), that also neglected the effects of magnetic field. Realistic simulations that take into account essential physics like non-local radiative transfer and an equation of state that adequately describes the solar plasma are needed to explain the observed properties of internal waves in the solar atmosphere. Theoretical work on MAG waves has been carried out by a number of authors, but atmospheric internal gravity waves in the presence of spatially intermittent and temporally evolving magnetic fields is a less explored field. Whether the presence of a magnetic field modifies the background properties and indirectly affects the propagation of internal waves or whether the changes in the plasma β and magnetic field orientation restrict the occurrence of internal waves to an even smaller region or perhaps suppresses them completely is still not clear. This paper addresses some of these aspects with state-of-the-art numerical simulations and attempts to fill some gaps in our understanding of atmospheric internal gravity waves.

The paper is structured as follows: In [Section 2](#), we discuss the numerical setup, the construction of the model, and give a detailed description of the properties of the non-magnetic and magnetic model in the context of internal waves. In [Section 3](#), we carry out a spectral analysis of the 3D simulation, where the emergent phase and energy flux spectra are presented, highlighting the differences between the two models. In [Section 4](#), we present a detailed discussion on the various effects that can explain the differences between the two models. The summary and conclusion of the paper is provided in [Section 5](#).

2. NUMERICAL MODELS

The numerical simulations of solar convection presented in this paper were carried out using the CO⁵BOLD code ([Freytag et al. 2012](#)). The code solves the equations of (magneto-)hydrodynamics for a fully compressible gas with a realistic equation of state, taking non-local radiative transfer into account. Here, we use five opacity groups, adapted from the MARCS stellar atmosphere package ([Gustafsson et al. 2008](#)). We take a 3D snapshot from an earlier model of relaxed convection, computed using CO⁵BOLD, and ex-

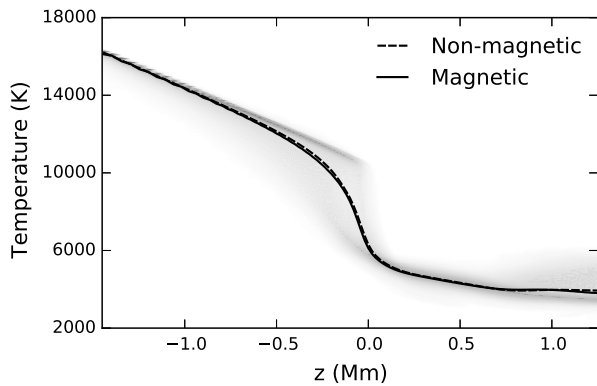
tend the domain by tiling it in the horizontal directions. The new computational domain has a size of 38.4 Mm \times 38.4 Mm \times 2.8 Mm, with a horizontal cell size of 80 km and a vertical cell size varying from 50 km in the lower part of the computational domain down to 20 km in the upper atmosphere, discretized on 480 \times 480 \times 120 grid cells. The domain reaches \sim 1.5 Mm below the level of average Rosseland optical depth $\tau_R=1$ (where we define the z axis such that $\langle z(\tau_R=1) \rangle = 0$) and \sim 1.3 Mm above it. A constant gravity of $g=275 \text{ m s}^{-2}$ acts in the box. The tiling results in a periodic pattern due to the previous periodic boundary condition. This pattern is eliminated by superimposing a random velocity pattern, with rms value of $0.5v_{x,y}$ (v_x and v_y are the horizontal components of the velocity), on the model between $z=-100$ and 0 km (below the average $\tau_R=1$ surface) over the entire horizontal scale and advancing the solution over several turnover timescale (approx. 190 min). Taking this solution as the initial model, a hydrodynamic (HD) and a magneto-hydrodynamic (MHD) simulation run is carried out. For the entire HD run, starting with the small domain, we use the Roe solver with VanLeer reconstruction (see [Freytag et al. 2012](#), for the details on the computational methods). The HLL-MHD solver with PP reconstruction is used for the MHD run ([Steiner et al. 2013](#)). For creating the MHD model, the extended initial HD model is embedded with a uniform vertical field of 50 G in the entire domain and advanced over a magnetic field redistribution timescale of approximately 600s. During this time the uniformly distributed fields are swept towards the inter-granular lanes by granular flow, forming localised flux concentrations with magnetic field strengths surpassing 1.5 kG at $z=0$ km. This model serves as a representation of an internetwork region of the quiet-Sun. The HD solution is advanced for the same duration to match with that of the MHD run. Both the hydrodynamic (“non-magnetic”) and magneto-hydrodynamic (“magnetic”) solutions are then advanced for 8 hours physical time with snapshots taken every 30 seconds. A summary of the numerical setup and physical properties of the two simulated models are shown in [Table 1](#).

Periodic boundary conditions are used for the side boundaries in both models. The velocity field, radiation, and the magnetic field components are periodic in the lateral directions, which results in the inhibition of waves with horizontal wavelengths larger than the width of the box. The top boundary is open for fluid flow and outward radiation, with the density decreasing exponentially in the boundary cells outside the domain. The vertical component of the magnetic field is constant across the boundary and the transverse component drops to zero at the boundary. In both models, the bottom boundary is set up in such a way that

Table 1. Numerical setup and physical properties of the two simulated models.

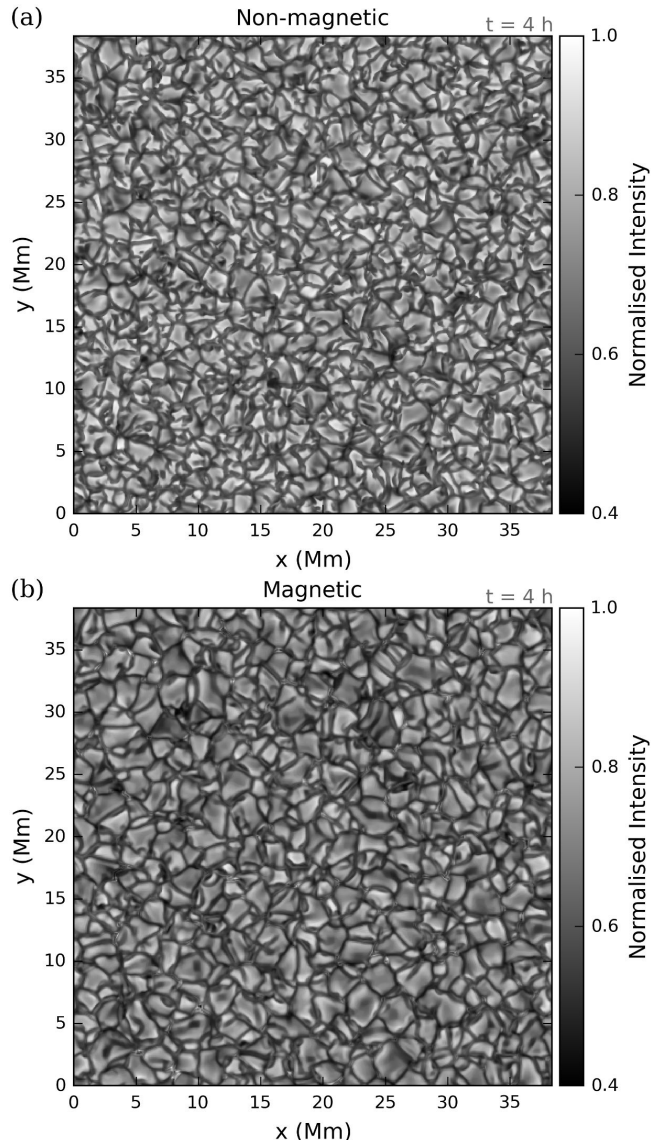
	Non-magnetic	Magnetic
Snapshot cadence	30 s	
Duration of simulation	8 hrs	
Computational grid	480×480×120	
Domain size	38.4×38.4×2.8 Mm ³	
Computational cell size	80×80×(50-20) ^a km ³	
Numerical scheme	Roe	HLL-MHD
Reconstruction	VanLeer	PP/VanLeer
Temperature, T_{eff}	5798±3 K	5773±4 K
Intensity contrast, δI_{rms}	15.57±0.13 %	15.32±0.11 %

^aThe vertical cell size varies from 50 km in the lower part of the computational domain down to 20 km in the upper atmosphere.

**Figure 1.** Average temperature as a function of height in the non-magnetic (dashed) and the magnetic (solid) model. The gray background shows the temperature distribution for a single snapshot of the non-magnetic run taken at $t=4\text{h}$.

the in-flowing material carries a constant specific entropy of $1.773 \times 10^9 \text{ erg g}^{-1} \text{ K}^{-1}$ resulting in a radiative flux corresponding to an effective temperature (T_{eff}) of $\sim 5770 \text{ K}$. The bottom boundary conditions for the magnetic fields are the same as for the top boundary.

The spatially and temporally averaged temperature profile of the two models is shown in Figure 1. Also shown in the background is the temperature distribution from a single snapshot of the non-magnetic model taken at $t=4\text{h}$ after the start of the simulation. Although the average temperature in the upper layers becomes constant, there are instances when the temperature increases locally, hinting to a weak shock-heated chromosphere. The two models show exactly the same temperature profile, but the granular sizes show slight differences. In Figure 2, we show the emergent bolometric intensity from the two models 4 hours after the start of the simulation. It is to be noted that, while the average size of granules in the non-magnetic model peaks at 2 Mm, the average granules in the magnetic model are larger. This is due to the more diffusive na-

**Figure 2.** Emergent bolometric intensity from: a) the non-magnetic and b) the magnetic model at $t=4\text{h}$.

ture of the HLL-MHD numerical solver, compared to the Roe solver. However, this difference between the non-magnetic and magnetic model does not seem to influence the overall spectra of the generated internal gravity waves as will be further explained in Sect. 5. The average rms bolometric intensity contrast, δI_{rms} , of the non-magnetic and magnetic models, are 15.57% and 15.31%, respectively (see Table 1).

The large spatial and temporal coverage of the two models give us the opportunity to study the different wave phenomena in Fourier space. All the physical variables are decomposed into their Fourier components along the horizontal directions and in time. In the following, we present the properties of the model in frequency-space for a better understanding of the different wave phenomena present in the simulation. The rest

of the paper is based on this decomposition and hence we attempt a detailed presentation.

2.1. The dispersion relation (k_h - ω diagram)

In an infinite, homogenous, compressible medium in the absence of an external force field, any small-amplitude perturbation propagates as acoustic wave owing only to the compressibility of the medium. The propagation is isotropic and non-dispersive with all the frequencies travelling at the characteristic sound speed (c_s) in all directions. In the presence of an external force like gravity, the propagation becomes anisotropic and acoustic waves are modified, with waves below a certain frequency becoming vertically non-propagative. Acoustic waves propagating horizontally, also called Lamb waves, are unaffected and therefore are non-dispersive. A continuously stratified fluid supplies a restoring force, in the form of buoyancy, resulting in the propagation of internal gravity waves. The coupling of the two waves in a compressible stratified medium, like that of the solar atmosphere, results in their separation into gravity-modified acoustic and compressibility-modified gravity waves. The two types of waves occupy distinct branches in the frequency-wave number domain (k_h - ω space) with a band of evanescent disturbance, separating the two branches. While, stratification results in a cut-off frequency for the acoustic waves, the effect of compressibility modifies the internal wave spectra at small horizontal wavenumbers ($k_h < 1/(2H_\rho)$, where H_ρ is the density scale height) from propagating. A detailed exposition on these waves is provided by [Lighthill \(2001\)](#).

The addition of magnetic fields to such a medium introduces waves due to the magnetic tension and pressure forces, that couple to the other waves already present in the medium, resulting in a spectrum of magneto-acoustic-gravity waves. Linearizing the full MHD equations about a uniformly stratified background state and assuming a wave-like solution, one obtains the dispersion relation for the magneto-acoustic gravity waves. Further assuming that the presence of a magnetic field just modifies the background atmosphere, the coupling to the magnetohydrodynamic waves can be neglected. The dispersion relation of the waves then reduce to (see [Priest 2014](#), for a derivation)

$$k_z^2 = \frac{(\omega^2 - \omega_{ac}^2)}{c_s^2} - \frac{(\omega^2 - N^2)k_h^2}{\omega^2}, \quad (1)$$

where ω is the frequency, k_h is the horizontal wavenumber ($k_h^2 = k_x^2 + k_y^2$), c_s is the adiabatic sound speed, ω_{ac} is the acoustic cut-off frequency, and N is the Brunt-Väisälä frequency, explained later in Equations (2) and (3).

The *local dispersion relation*, given by Equation (1), separates the wave-behaviour in the k_h - ω diagram also

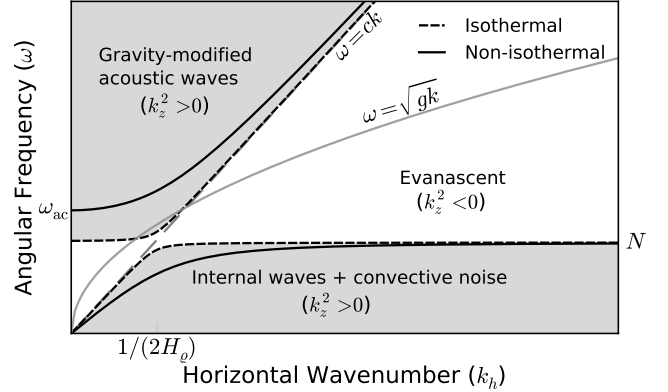


Figure 3. Schematic diagram showing different regimes of wave propagation in a compressible, gravitationally stratified medium for a given height in the atmosphere. The shaded area marks regions of vertical propagation of acoustic and the gravity waves. The propagation boundaries separate the vertically propagating ($k_z^2 > 0$) from the evanescent ($k_z^2 < 0$) solutions. The solid curve represents the propagation boundaries obtained from the non-isothermal cut-off frequencies defined in Equations (2) and (3). The dashed curves are obtained when we use the isothermal approximation for ω_{ac} . The dispersion relation for the surface-gravity wave is shown in gray. The long dashed gray line corresponds to the dispersion relation for the Lamb waves.

known as the diagnostic diagram. The two regions of propagation in the k_h - ω diagram are obtained by setting $k_z^2 = 0$ in Equation (1) (see e.g., [Leibacher & Stein 1981](#)), with the $k_z^2 > 0$ domain isolating the vertically propagating solution from the evanescent region ($k_z^2 < 0$). A schematic of such a diagnostic diagram for a compressible, gravitationally stratified medium for a given height in the atmosphere is shown in Figure 3.

For small k_h ($< 1/(2H_\rho)$), the lowest frequency with which a gravity-modified acoustic wave can propagate upward is limited by the acoustic cut-off frequency ($\omega_{ac} = c_s/(2H_\rho)$), which, for an isothermal atmosphere, is a function of the sound speed and the density scale height (H_ρ), referred to as the Lamb frequency. However, in the non-isothermal case like that of the solar atmosphere, the gradients in temperature modify the cut-off frequency. While there are different expressions for the cut-off frequency, depending on different representations of the wave equation ([Mosser 1995](#); [Schmitz & Fleck 1998](#)), in this paper, we adopt the one due to [Deubner & Gough \(1984\)](#), viz.,

$$\omega_{ac}^2 = \frac{c_s^2}{4H_\rho^2} \left(1 - 2 \frac{dH_\rho}{dz} \right), \quad (2)$$

which is obtained when the wave equation is cast in terms of $\rho^{1/2} c_s^2 \nabla \cdot v$ as the oscillating function. The difference in the diagnostic diagram between the isothermal and the non-isothermal case for a particular height in the atmosphere is also shown in Figure 3.

Internal waves exist below the acoustic cut-off fre-

quency and have horizontal phase velocity less than the sound speed in the medium. The maximum frequency of propagation for internal waves is set by the Brunt-Väisälä frequency (N), also called the stratification or buoyancy frequency. For a non-isothermal atmosphere, it is defined as,

$$N^2 = g \left(\frac{1}{H_\theta} - \frac{1}{\gamma H_p} \right), \quad (3)$$

where, γ is the ratio of the specific heats (c_P/c_V). Recalling that the pressure scale height (H_p) is equivalent to the density scale height (H_ρ) in an isothermal atmosphere, the expression for the Brunt-Väisälä frequency in an isothermal case can be recovered. In the presence of a magnetic field, the Brunt-Väisälä frequency can be further modified, but we do not consider this effect here.

A fluid element vertically displaced from its equilibrium position will oscillate and emit gravity waves provided the background atmosphere satisfies the Schwarzschild criterion for stability ($N^2 > 0$). If there are local departures from the stability criterion due to the overshoot material in a stable stratified surrounding, the fluid element becomes unstable and rises up, cools down by radiating and falls back, completing the convective cycle. In observations, the frequency range covering the internal waves is dominated by the convective noise, but the propagation properties of the internal waves have been studied by carrying out a phase spectra analysis of these waves.

We have presented the diagnostic diagram and the significance of distinguishing the two-wave behavior in such a diagram. In the following section, we will look at the analysis of the simulation data based on this diagnostic diagram.

3. SPECTRAL ANALYSIS

The complex cross-spectrum of two real-valued processes: $f(\mathbf{x}, t)$, $g(\mathbf{x}, t)$, is defined as:

$$\begin{aligned} \mathcal{S}_{f,g}(\mathbf{k}, \omega) &\equiv \mathcal{C}_{f,g}(\mathbf{k}, \omega) + i\mathcal{Q}_{f,g}(\mathbf{k}, \omega), \\ &= \mathcal{F}(\mathbf{k}, \omega) \overline{\mathcal{G}(\mathbf{k}, \omega)}. \end{aligned} \quad (4)$$

$\mathcal{F}(\mathbf{k}, \omega)$ and $\mathcal{G}(\mathbf{k}, \omega)$ are the Fourier transforms of the two processes, with the overbar representing the complex conjugate. The real part of \mathcal{S} is known as the co-spectrum (\mathcal{C}), and gives the correlation of the in-phase/anti-phase Fourier components (\mathbf{k}, ω) of the two processes. The imaginary part of \mathcal{S} is known as the quadrature spectrum (\mathcal{Q}) and represents the correlation of the out-of-phase Fourier components between the two processes (Hayashi 1982). These quantities will be further explored in the context of energy fluxes of the internal waves discussed in Section 3.2.

Using the cross-spectrum, the phase lag or the phase difference between the two processes is formally given

as,

$$\phi_{f,g}(\mathbf{k}, \omega) = \tan^{-1} \left[\frac{\mathcal{Q}_{f,g}(\mathbf{k}, \omega)}{\mathcal{C}_{f,g}(\mathbf{k}, \omega)} \right], \quad (5)$$

where, $\phi(\mathbf{k}, \omega)$ is known as the phase difference spectrum, or simply the phase spectrum. However, Equation (5) gives reliable phases only if the two processes are linearly dependent for a given Fourier component. The linear dependence of the two processes is measured by the coherence spectrum (\mathcal{K}), defined as,

$$\mathcal{K}_{f,g}^2(\mathbf{k}, \omega) = \frac{\mathcal{C}_{f,g}^2(\mathbf{k}, \omega) + \mathcal{Q}_{f,g}^2(\mathbf{k}, \omega)}{\mathcal{S}_{f,f}(\mathbf{k}, \omega) \mathcal{S}_{g,g}(\mathbf{k}, \omega)}, \quad (6)$$

with $\mathcal{S}_{f,f}$ representing the auto-spectrum of process f and $\mathcal{S}_{g,g}$ representing the auto-spectrum of process g , according to Equation (4). The phase spectra, together with the coherence spectra give an estimate of the phase-difference between the two processes, with $\mathcal{K}=1$, when the two processes are linearly related, and $\mathcal{K}=0$, when no linear dependence exists for the given Fourier component.

In our analysis, the components of velocity and various other thermodynamic quantities are extracted from the two models for the entire duration of the simulation. We then carry out the analysis in the three-dimensional Fourier space by transforming the data cube of the derived quantities consisting of two horizontal spatial (x, y) and one temporal (t) direction, using Fast Fourier Transform (FFT). This is done so for each horizontal plane of the vertical coordinate grid (the z axis) to obtain a four-dimensional data set of the relevant quantities on a (k_x, k_y, ω, z) grid. The derived quantities are then represented on a k_h - ω diagram for each height level by azimuthally averaging over the k_x - k_y plane. With the domain spanning 38.4 Mm in the horizontal directions and 8 hours long, we have a spectral resolution of 0.164 Mm^{-1} in horizontal wavenumber and $138 \mu\text{Hz}$ in frequency. The grid resolution of 80 km results in a Nyquist wavenumber ($k_{N_y} = \pi/\delta x$) of 39.25 Mm^{-1} of which we are only interested in horizontal wavenumbers below 8 Mm^{-1} , where the bulk of IGWs occur. A vertical and horizontal grid constant of respective 20 km and 80 km is sufficient to capture the range of the internal wave spectrum in the models as will be discussed in Sect. 4. Snapshots from the simulations were taken at 30s interval resulting in a Nyquist frequency (ν_{N_y}) of 16.66 mHz. Since the Brunt-Väisälä frequency in the atmosphere is typically below 5 mHz, we show in the following only the analysis up to the frequency range of 8 mHz.

3.1. Phase and coherence spectra

Acoustic waves and internal waves have different polarization properties and therefore show different behaviour in their phase spectra. Unlike for acoustic

waves, the velocity fluctuations of internal waves and therefore the energy transport (ray path) of the wave is perpendicular to the wave vector \mathbf{k} . Moreover, the wave vector is always directed towards the plane of the source of perturbation that excited the wave (see e.g., Sutherland 2010). Hence, an internal wave transporting energy at an angle to the vertical, with an upward component, will have a downward propagating phase component which shows up as negative phase lag between two geometrical heights. This behaviour can be clearly identified by computing the phase spectra obtained from velocity measurements at two different heights. The diagnostic potential of the phase and coherence diagram was explored in a series of papers by Deubner & Fleck (1989), Fleck & Deubner (1989), Deubner & Fleck (1990), Deubner et al. (1990), and Deubner et al. (1992). These have been used to separate out the internal wave signature from the low frequency convective noise.

In the following, we look at the velocity-velocity (v - v) phase spectra, which shows the phase lag between the velocities measured at two different heights. The v_z - v_z phase spectra are determined from the vertical component of the velocity for a pair of heights as described in the beginning of Section 3 and represented in the form of the diagnostic diagrams. While phase spectra determined from observations of the solar atmosphere rely on spectral lines formed over a particular height range, in this work we focus only on phase spectra obtained from pairs of plane parallel, geometrical height levels. Figure 4 shows the v_z - v_z phase spectra for pairs of heights for the non-magnetic (left panels) and for the magnetic (right panels) model of Table 1. In order to better understand the effect of magnetic fields on the propagation of internal waves, we study the phase spectra obtained from three carefully selected pairs of heights. These heights are chosen in such a way that they probe three regions of interest in the magnetic case. The colors represent the phase differences (ϕ) and the shading represents the coherency (\mathcal{K}), with corresponding colorbars shown on the right of the plots. Positive phases (upward) are represented with a progressively yellow to red color-scale and the negative phases (downward) are shown with a green to blue color-scale. The shading scale for the coherency is shown on the top of the colorbar. The gray curve in each plot shows the dispersion relation of the surface gravity waves. The dashed and solid curves correspond to the propagating boundaries of the two wave branches at the lower and the upper height, respectively.

The first pair of heights, $z=100$ km and $z=240$ km, lies close to the surface, where the internal waves are thought to be excited by overshooting convection. In the magnetic model, this height range probes a gas-dominated part of the atmosphere ($\beta>1$, where β is

the ratio of the gas pressure to the magnetic pressure). The diagnostic diagram of these two heights is shown in Figure 4a, where we see that both models have generated significant amounts of internal waves, which show up as downward phases in the internal gravity wave-regime of the diagnostic diagram (the green area below the lower dashed curve that show phase difference of around -10° over a height difference of 140 km). Although, the generation of the internal waves and how magnetic fields influence the generation is of great interest, we defer such a study to a later paper. Here, we focus only on the propagation properties of these waves in the presence of magnetic fields. As can be seen, the downward phases are restricted to the region below the dashed curve, suggesting that the excited internal waves are propagating only below the boundary determined by the lowest Brunt-Väisälä frequency (in this case, the N of the lower height).

The two spectra of the excited internal waves in Figure 4a are qualitatively the same regardless of whether being generated in the convective or magneto-convective model. It should be noted that the magnetic model, however, inhibits surface gravity waves, the spectrum of which is clearly seen as a green ridge extending along the gray curve in the non-magnetic model. This could be due to the fact that the magnetic fields in the simulation box are predominantly vertical so that the propagation of the nearly horizontal surface gravity waves are hindered by their presence.

Now we turn to Figure 4b, the second pair of heights ($z=140$ km and 600 km), which are still within predominantly gas dominated regions ($\beta>1$). But, in the atmosphere that these heights probe, the surfaces of constant plasma- β are rugged with occasional strong magnetic fields dipping the plasma- β surfaces. The non-magnetic model shows the signature of internal waves with the downward phases with phase differences of around -90° over a height difference of 460 km. In the magnetic model they are significantly reduced, suggesting that the magnetic fields have a major influence on the internal waves as they propagate upwards. Here again, the negative phase difference, and therefore the propagating region in the diagnostic diagram is mainly below the boundary set by the N of the lower height. Also note that the coherence has reduced as evident from the increased shading for the larger wavenumbers, since we are probing heights separated by a larger distance. The surface-gravity waves (ridge along the gray curve), on the other hand, are still present in the non-magnetic model, but they are completely absent in the magnetic model.

Figure 4c refers to the third pair of heights ($z=560$ km and 900 km), where the first height is in a gas dominated region ($\beta>1$) and the second height is in the magnetic

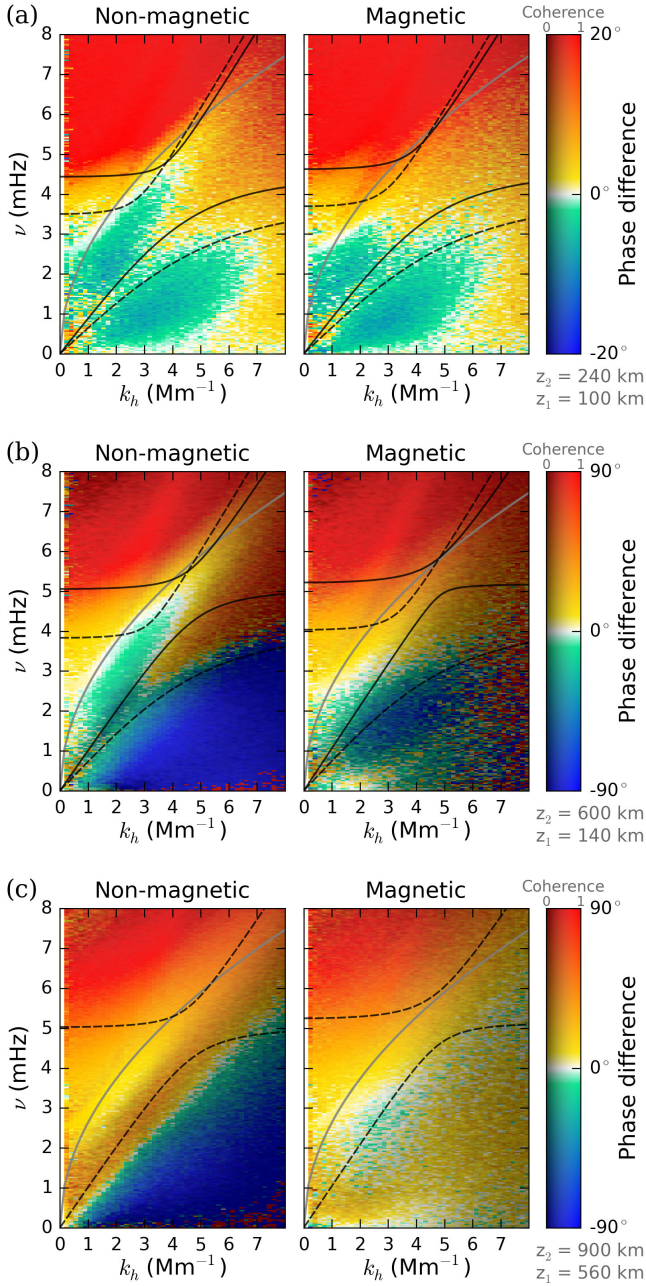


Figure 4. v_z - v_z phase spectra estimated between: a) $z=100$ km and $z=240$ km; b) $z=140$ km and $z=600$ km; and c) $z=560$ km and $z=900$ km, for the non-magnetic model (left) and the magnetic models (right). The dashed black curves represent the propagation boundaries obtained from the non-isothermal cut-off frequencies defined in Equations (2) and (3) for the lower height and the solid curves correspond to the upper height. The gray curve is the dispersion relation of the surface-gravity waves. The colors represent the phase differences (ϕ) and the shading shows the coherency (\mathcal{K}).

field dominated region ($\beta < 1$). We see that most of the internal waves are absent in the magnetic model (phase difference of 0° over a height difference of 340 km). Some regions of the diagnostic diagram in the internal wave regime of the magnetic model also show positive phase differences (upward propagating phases) of around 10° . According to their polarisation properties, this suggests that the wave energy is propagating downwards in the atmosphere.

In summary, the non-magnetic case shows a strong negative phase difference in the internal wave region in all three pairs of heights, while the magnetic case shows a clear signature of upward propagating internal waves for the pair of heights in the lower atmosphere and mostly zero to positive phase differences in the upper atmosphere. From the above analysis, we observe that the presence of nearly vertical magnetic fields influences internal waves and it results in their suppression or partial reflection in the atmosphere. There are several ways by which internal waves can behave this way, and we explore some of these factors in Section 4 to understand the behaviour that we see in our simulation.

3.2. Energy flux spectra

The phase spectrum analyses show that in the case of the magnetic model the internal waves are absent or even show a positive phase difference because they propagate down in the higher layers. This means that in this case they are either destroyed or reflected back and are transporting their energy downwards, unlike the acoustic waves which mainly transport their energy upwards in the atmosphere. An estimate of the energy flux spectra can shed some light on the actual energy transport by internal waves in the presence of magnetic fields.

A propagating wave transports energy to the far field, when pressure and velocity oscillate in-phase. In order to estimate the vertical component of the linearized mechanical energy flux of these waves, we look at the co-spectrum of the pressure fluctuations, Δp , and the vertical component of the velocity, v_z (Lighthill 2001), averaged over one wavelength ($1/2$ factor). As described at the beginning of Sect. 3, the co-spectrum gives us the in-phase cross-spectrum, which in this case, is the active mechanical energy flux transported by the waves,

$$\begin{aligned}
 F_M(\mathbf{k}, \omega) &= \frac{1}{2} \mathcal{C}_{\Delta p, v}(\mathbf{k}, \omega), \\
 &= \frac{1}{2} \text{Re}[\Delta p(\mathbf{k}, \omega) \overline{v(\mathbf{k}, \omega)}]. \quad (7)
 \end{aligned}$$

The energy flux, F_M , calculated using Equation (7) in the k_x - k_y plane is then azimuthally averaged and represented on the diagnostic diagram. Figure 5a and 5b shows the energy flux spectra computed at a height of $z=360$ km and $z=700$ km, respectively. Positive values

correspond to upward flux and negative values correspond to downward flux. The energy flux spectra computed for $z=360$ km (see Figure 5a) show that both the acoustic and the internal waves transport their energy upwards in both the magnetic and non-magnetic model. When we look at the energy flux spectra at $z=700$ km (see Figure 5b), it is clear that the internal waves in the non-magnetic model still carry a positive flux, which means they are propagating and transporting energy predominantly upwards. However, the magnetic model shows a mixture of positive and negative energy flux in the gravity wave regime (in locations where there is a negative phase difference in the right panel of Figure 4b), suggesting that at this height, the waves are propagating in both directions up and down, and thus energy is transported in both directions. The upward propagating waves are probably the one that are generated in the lower atmosphere, and the downward propagating waves are the one reflected from the top layer of the atmosphere.

In this work, we have not attempted to compute the Poynting flux from the magnetic model, as we cannot do a comparative study with the non-magnetic model. Future work will explore the emergent Poynting flux by comparing different magnetic models.

4. DISCUSSION

We now focus our attention on explaining the behaviour of internal waves that are seen in the numerical models, particularly the absence or the downward propagation in the magnetic model, which is also partially evident from the energy flux spectra. We explore different factors that may affect the propagation of internal waves in a realistic atmosphere. All the factors considered below can restrict the possible height range over which internal waves can occur in the solar and, generally, in stellar atmospheres. We start by looking at the differences in the height dependence of the diagnostic diagram in both models and how this affects the propagation of internal waves, followed by the influence of radiative damping and non-linear effects and finally the presence of magnetic fields. We will see that, while the lower and upper limiting boundaries of the internal wave cavity are determined by the radiative damping effects and flow parameters, respectively, the propagation within the allowed domain is strongly influenced by magnetic fields.

We note that the effect of numerical diffusion becomes important at the level of a couple of grid cells only. The artificial diffusion in CO⁵BOLD is invoked at shock fronts or for waves with large amplitudes, where strong gradients of velocity exist. Since gravity waves do not shock or do not steepen very much, they are not affected by artificial numerical diffusion; it influences

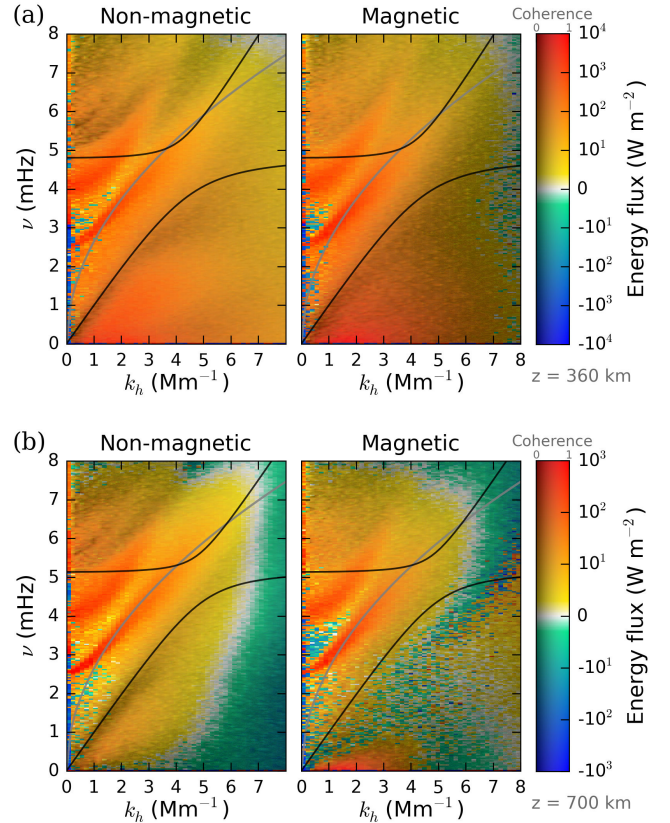


Figure 5. Energy flux spectra at heights of a) $z=360$ km and b) 700 km of the non-magnetic model (left) and the magnetic model (right). The solid black curves represent the propagation boundaries obtained from the non-isothermal cut-off frequencies defined in Equations (2) and (3). The gray curve is the dispersion relation of the surface-gravity waves.

waves of short wavelengths only, which, however, are irrelevant in this study since we see the effects of magnetic fields mainly at long wavelengths. Also, current observations of IGWs do not have the spatial resolution to detect power at such short wavelengths. On the other hand, since in our models the horizontal wave number of the propagating IGWs is smaller than 7 Mm^{-1} (see Fig. 4a), which corresponds to wavelengths larger than ≈ 1000 km, they are well resolved with the horizontal grid spacing of 80 km. Likewise, in the vertical direction, Fig. 4a together with Eq. (1) tells us that $k_z < 40 \text{ Mm}^{-1}$ corresponding to wavelengths larger than ≈ 160 km, which are well resolved with the present vertical grid spacing of 20 km.

4.1. Variation of the diagnostic diagram with height

In the case of a convectively stable, uniformly stratified atmosphere, N^2 is positive and constant and an internal wave can freely propagate throughout the atmosphere. However, in a more realistic atmosphere like the one we simulate, N varies with height. Variations or dis-

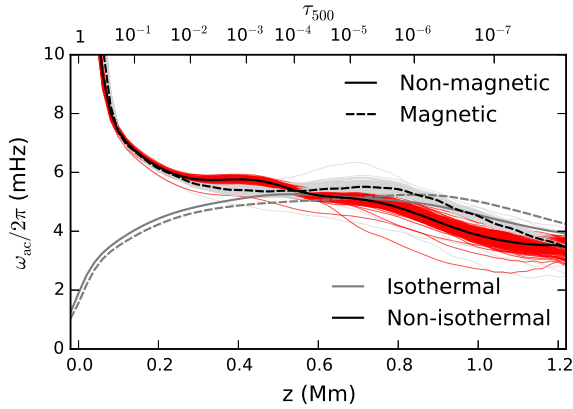


Figure 6. Temporally and horizontally averaged isothermal (gray curves) and the non-isothermal (black curves) acoustic cutoff (ω_{ac}) frequency as a function of height in the non-magnetic (dashed) and the magnetic (solid) model above $z=0$ km. The gray and red scatter indicate the temporal variation of the non-isothermal acoustic cut-off for the non-magnetic and the magnetic simulations, respectively.

continuities in N result in partial reflection or trapping (ducting) of internal waves within the domain. As we have seen in Section 2.1, a spectral band of evanescent disturbances (white region in Figure 3) separates the gravity-modified acoustic waves from the internal gravity waves (gray region in Figure 3). Waves with a specific (k_h, ω) that fall in either of these two gray regions in the diagnostic diagram, of a certain height, have oscillatory solutions at that particular height and propagate as waves with their characteristic nature. All other combinations of (k_h, ω) are evanescent in the atmosphere. The parameters that set these limits are mainly ω_{ac} and N , which vary as a function of height in the real solar atmosphere leading to changing wave behaviour, i.e, a changing diagnostic diagram with height.

Figure 6 shows the time-averaged ω_{ac} as a function of height in the two simulations that are presented in this paper (black curves). The variation of ω_{ac} is the result of the changing temperature and stratification. The ω_{ac} for the iso-thermal case is shown in gray which takes into account only the local sound speed and density scale height. Figure 7 shows the time-averaged N as a function of height in the two simulations. The time-averaged N for the isothermal case is shown in gray. In both figures, the gray and red scatter show the temporal variation of the non-isothermal value for the non-magnetic and magnetic models, respectively.

In order to fully understand the propagation and transport of energy by the two types of waves, it is important to know the local diagnostic diagram as a function of height and thus the critical frequencies as a function of height, as shown in Figures 6 and 7. Oscillating solutions to the wave equation for a particular (k_h, ω) may exist over the entire domain or only for a particular

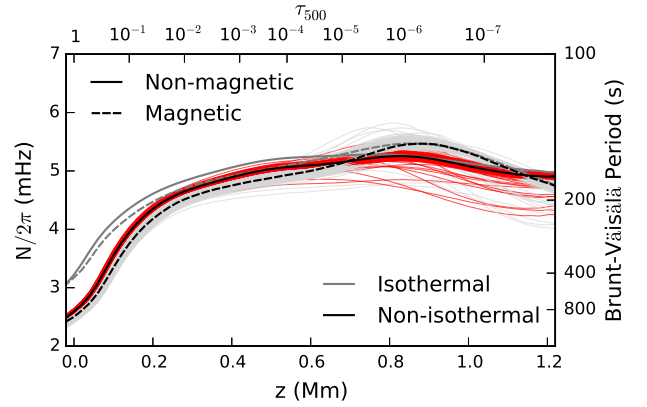


Figure 7. Temporally and horizontally averaged isothermal (gray curves) and the non-isothermal (black curves) Brunt-Väisälä frequency as a function of height in the non-magnetic (dashed) and magnetic (solid) models above $z=0$ km. The gray and red scatter indicate the temporal variation of the non-isothermal Brunt-Väisälä frequency for the non-magnetic and the magnetic simulations, respectively.

range of heights. A wave at a particular height with a frequency that falls in the white region in Figure 3 is partially *reflected* at the respective limits, as discussed in connection with Equation (1), beyond which it becomes *evanescent*. If such a limit exists at another height for the same wave, and a propagating wave solution exist for the region between these two heights, then the wave is said to be *trapped*. On the other hand, if oscillatory solutions exists on either side, then the waves can *tunnel* through this barrier. Following the above criterion for the range of wavelengths present in our simulation, the diagnostic diagram can be separated into different regions for each branch of the acoustic-gravity spectrum.

According to Figure 7 it is clear that the propagating branch of internal waves occupy nearly the same region of the k_h - ω diagram in both models, because N as a function of height is almost identical. A wave that propagates into a region where it has no oscillatory solution is partially reflected back towards the propagating region, the rest becoming evanescent on the opposite side. In our models, these reflecting surfaces for the internal waves occur in the low photosphere where N sharply drops with depth¹ (see Figure 7). Trapped internal waves in our model occupy a very small region in the k_h - ω diagram with frequencies close to the maximum N in the entire box. Since these waves have frequencies close to N , their phases propagate almost horizontally, transporting their energy upwards, which makes them

¹ Mihalas & Toomre (1981) considered a 1D atmosphere with effects of ionization and external forcing due to “turbulent pressure” which causes a decrease in N with height having the consequence that the bottom of the chromosphere acts as a reflecting layer for waves propagating upwards.

important for energy transport to the upper atmosphere. However, the range of frequencies that are trapped is very small in both our models, lying within the concave stretch of N from $z=0.4$ Mm to 1.2 Mm in Figure 7. This is small compared to previous work, which considered a larger height range with a sharp decrease in N with height.

From Figure 7 it is evident that the reflection that we observe in the magnetic model cannot be not due to the variation of N with height because N remains nearly constant higher up in the atmosphere. In our specific case, we have only the lower part of the atmosphere acting as a reflecting layer for the internal gravity waves propagating downwards and the non-magnetic and magnetic model show a similar variation of N with height.

4.2. Radiative damping

Internal waves are thought to be generated by overshooting convection into the stably stratified layer above. While, the lower boundary for the waves to exist is determined by the positivity of N^2 (which is the condition for a convectively stable region), radiative effects play an important role in damping the waves higher up in the atmosphere. Near the surface, the radiative relaxation time, τ_{rad} , defined in the optically thin limit as (Spiegel 1957),

$$\tau_{\text{rad}} = \frac{\rho c_V}{16\kappa\sigma T^3}, \quad (8)$$

drops sharply to values of seconds. Thus temperature fluctuations are smoothed out on comparable timescales. However, τ_{rad} rapidly increases with height again, so that radiative effects have no influence on the propagation of internal waves in the layers above the mid-photosphere. Internal waves with periods larger than τ_{rad} are destined to be strongly damped in the near surface layers. The effect of radiative damping on internal waves has been extensively studied by Mihalas & Toomre (1982), who consider a simple linear height dependent Newtonian cooling and assume different initial energy fluxes for the waves.

The damping ratio, $1/2N\gamma\tau_{\text{rad}}$, characterises the effect of radiative damping of internal waves. Figure 8 shows the damping ratio as a function of height in both our models. Also shown in gray is the approximation used by Mihalas & Toomre (1982) for comparison. It can be clearly seen from the plot that the gravity waves undergo heavy radiative damping below a height of 0.2 Mm, where the damping ratio is above 1. However, the waves are unaffected by radiative damping higher up in the atmosphere.

In the lower atmosphere, it is clear from the phase spectra that we still see signatures of upward propagating internal waves, despite strong radiative damping. It

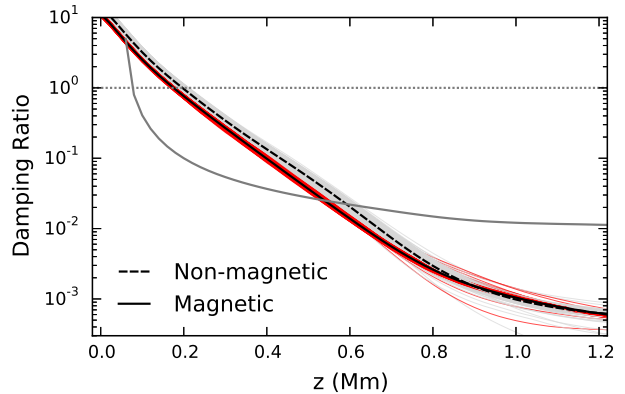


Figure 8. Damping ratio as a function of height in the non-magnetic (dashed) and magnetic (solid) model. The gray and red scatter indicate the temporal variation of the damping ratio for the non-magnetic and the magnetic simulation, respectively. The gray curve represents the approximation used by Mihalas & Toomre (1982).

seems that the internal wave flux generated by the convective overshooting is still strong enough so that a significant amount of internal waves survive (see Figure 4a) in regions where the damping ratio is above 1. Non-local radiative transfer can have an inverse effect in the sense that instead of smoothing, the spatial temperature fluctuations are enhanced, as was conjectured by Mihalas & Toomre (1982) which needs to be further investigated.

4.3. Non-linear interaction

Internal waves dissipate their energy by breaking into turbulence. In a large eddy simulation like the one that we carry out here, wave breaking is very limited. Nevertheless, it is worthwhile to have an estimate of the effect of different processes that may lead to the breaking of internal waves into turbulence, or forming critical layers. A ‘critical level’ is defined as the level at which the mean flow speed becomes comparable to the horizontal phase speed of the wave. The most important among them is the effect of a background flow, like the presence of a strong shear flow or vorticity. In the case of a background plane-parallel shear flow, the height at which the horizontal phase speed becomes comparable to the background flow speed, will act as a critical layer resulting in the reflection of waves. The importance of shear flows for gravity waves can be characterized by the Richardson number (Ri), defined as,

$$\text{Ri} = N^2 / \left(\frac{dv_h}{dz} \right)^2, \quad (9)$$

where v_h is the horizontal component of the velocity. The estimated value of Ri in our model atmosphere is everywhere larger than 0.25 (see e.g., Lindzen 1988), suggesting that the atmosphere is dynamically stable and shear flows that are strong enough to lead to dynamical instabilities do not exist.

Another stability condition considered by [Mihalas & Toomre \(1981\)](#) is the ratio of the wave vorticity, ζ , and N . Figure 9 shows the ratio of the average fluid vorticity and N as a function of height. We find that the ratio, ζ/N , is small in both models above 0.1 Mm, suggesting that instabilities do not develop as a result of the flow vorticity in our models. Note however, that ζ/N is larger and increases with height in the magnetic model compared to the non-magnetic model, probably because of the generation of vorticity by the magnetic field in the low- β regime ([Shelyag et al. 2011](#); [Steiner & Rezaei 2012](#); [Wedemeyer-Böhm et al. 2012](#)). We also observe that the vortices in the non-magnetic model near the surface are larger compared to the magnetic model as also reported in observations by [Sangeetha & Rajaguru \(2016\)](#).

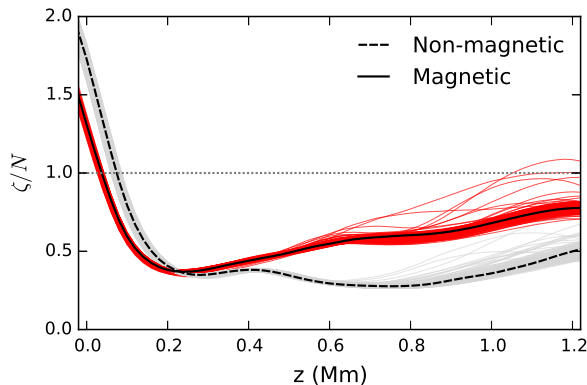


Figure 9. Non-linearity parameter (ζ/N) as a function of height in the non-magnetic (dashed) and magnetic (solid) models. The gray and red scatter indicate the temporal variation of the ratio ζ/N for the non-magnetic and the magnetic simulation, respectively.

We recall that the simulations presented in this paper were carried out on a coarse grid of 80 km cell size in the horizontal directions which only marginally captures the development of strong vortical flows. Having a higher spatial resolution may likely result in vortical flows having a stronger effect on the internal waves. In fact, high-resolution simulations with a smaller box size than the one presented here shows that ζ/N rises above 1 in the top layers where magnetic fields are present. As can be seen in the Figure 9, there are instances when the ζ/N increases and strides above 1 close to the top boundary in the magnetic model. This implies that vortical motions must be considered a possible reason why internal waves are absent in the magnetic model.

4.4. Linear mode coupling

The presence of magnetic fields itself may play a significant role in modifying the nature of internal waves in places where they exist. [Newington & Cally \(2010, 2011\)](#)

considered internal wave propagation in a VAL-C solar reference atmosphere, containing a uniform magnetic field with different field inclinations. Using generalized ray theory and with the help of linear simulations, they show that the internal waves are reflected within the region where plasma $\beta > 1$, and convert to downwardly propagating slow waves (predominantly magnetic in nature). The presence of strongly inclined fields (with an inclination of 80° or more) in these regions can modify the waves and convert them to acoustic (in case of 2D) or Alfvén waves (in case of 3D) and guide them along the field lines with radiative damping playing only a minor role ([Newington & Cally 2011](#)).

In more realistic simulations like the one we consider in this paper, it is difficult to specify an average height of the plasma $\beta=1$ surface or a characteristic inclination of the magnetic fields. The magnetic fields are continuously shuffled and reformed in the inter-granular lanes forming a complex structure as shown in Figure 10. In order to show how the plasma $\beta=1$ surface or the magnetic field inclination vary, we compute the average values of β , the sound speed, c_s , the magnitude of the Alfvén velocity, v_A , the vertical component, B_v , and the horizontal component of magnetic field, B_h , given as $B_h^2 = B_x^2 + B_y^2$ over the entire simulation run as a function of height. Figure 11 shows the plasma β (dashed) and the ratio of c_s to v_A (solid), as a function of height, averaged over horizontal planes and in time over the entire simulation. Also shown is the temporal scatter of c_s/v_A (light gray) and of plasma β (red). From Figure 11, it is evident that the domain below $z=0.8$ Mm is gas dominated, although there are localized regions of strong magnetic field that dip the β surface down to $z < 0$. According to [Newington & Cally \(2010\)](#), internal waves in our model are less likely to be present above $z=0.7$ Mm as most of them will undergo conversion to slow (predominantly magnetic) waves and reflect back before reaching this height.

Our simulation also shows a significant horizontal component of the magnetic field at photospheric heights, in agreement with recent observations of the solar atmosphere ([Lites et al. 2008](#); [Orozco Suárez & Bellot Rubio 2012](#)). Figure 12 shows the average horizontal (solid curve) and vertical component (dashed) of the magnetic field along with the average field inclination (dotted) and its temporal scatter shown in gray. The vertical component of the magnetic field dominates in the entire domain mainly due to the relatively strong (50 G) uniform vertical field, of the initial configuration. However, the fields tend to be inclined around 0.5 Mm, with a maximum average inclination of 40° , which can act as a portal for internal waves to escape into the layers above and convert to acoustic and Alfvén waves. This conversion is highly dependent on the field angle and

the model that we have does not have strongly inclined fields (fields above an inclination of 80°) to facilitate this pathway. From the phase spectrum analysis, we do not see a strong transmission of the internal waves into the upper atmosphere (see Figure 4b,c right panels). We can conclude that most of the waves sense the $c_s=v_A$ surface and are reflected back within the high- β region, but we cannot say if it is due to mode coupling or non-linear shear flow interaction.

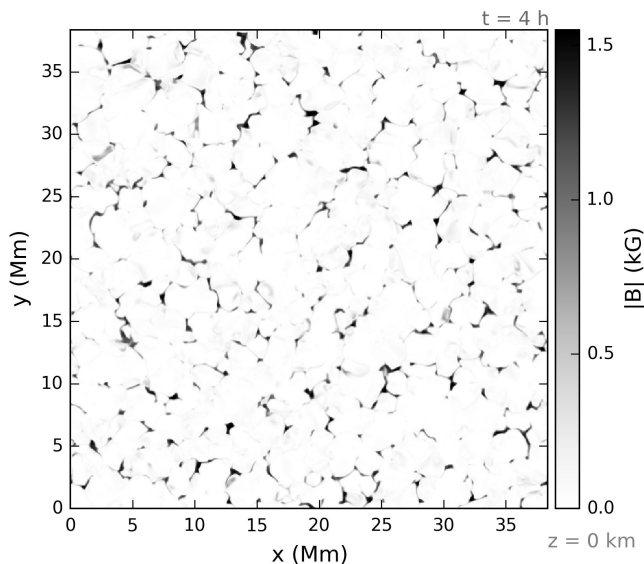


Figure 10. Snapshot of the absolute magnetic field strength, $|B|$, at $t=4$ h in the simulation, taken at $z=0$ km.

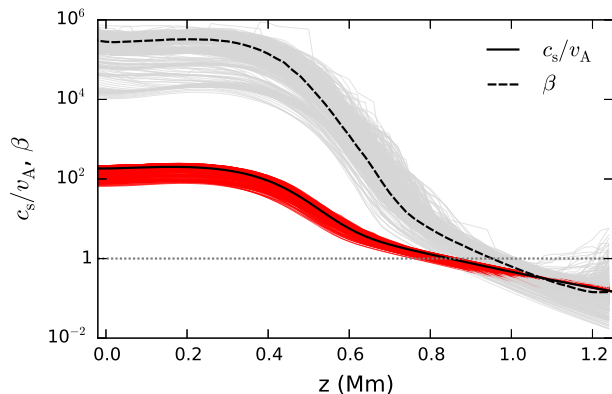


Figure 11. Temporally and horizontally averaged ratio c_s/v_A (solid curve) and plasma β (dashed curve) in the magnetic simulation. The red and gray scatter show the temporal variation of c_s/v_A and plasma β , respectively.

5. SUMMARY AND CONCLUSION

Internal gravity waves in the solar atmosphere are thought to be generated mainly by the overshooting of convective matter into the stably stratified atmosphere lying above. Strong radiative cooling in the immediate

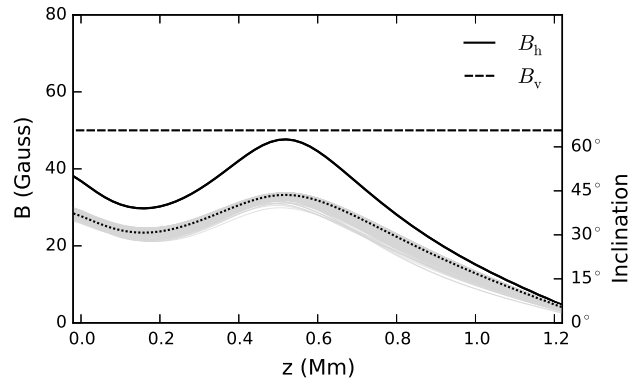


Figure 12. Temporally and horizontally averaged components of the magnetic field in the magnetic simulation. The vertical field is shown as a dashed curve and the horizontal field is shown as a solid curve. The dotted curve shows the average inclination of the field from the vertical, and the gray curves show the temporal scatter of the average inclination.

vicinity of the solar surface causes these waves to quickly damp, but they are believed to be present higher up in the atmosphere where the radiative timescales are large. Theoretical studies show that the flow field higher up in the atmosphere may lead to the breaking of internal waves to turbulence resulting in a complete dissipation of their energy in the mid-chromosphere, before even reaching to coronal heights. Additional complications are brought about by the presence of magnetic fields in this region, questioning their ability to transport energy in the solar atmosphere at all. A clear understanding of the gravity-wave phenomena occurring in the lower solar atmosphere requires a comprehensive treatment in three dimensions, including the effects of magnetic fields, non-local radiative transfer and realistic equation of state.

In this paper, we have presented a study of the acoustic-gravity wave spectrum emerging from a realistic simulation of solar convection. A purely hydrodynamic and a MHD simulation were carried out to highlight the effect of the magnetic fields on the propagation of internal waves. The generated internal waves in both models are studied in the spectral-domain by looking at the emergent phase spectra between two heights in the atmosphere and estimating the energy flux spectra. These studies were carried out in the light of the observations by [Straus et al. \(2008\)](#) that the gravity waves are suppressed at locations of magnetic flux. These authors assumed that the suppression is a result of mode conversion of internal waves to Alfvén waves.

Our analysis shows that the internal waves are generated in both models and overcome the strong radiative damping in the lower photosphere to propagate into the higher layers. The radiative damping is strong below $z=200$ km but the phase difference spectra show signatures of these waves even below this height, suggesting that the mechanism generating them efficiently imparts

enough energy to the wave to overcome the strong radiative damping. But the magnetic fields affect these waves as they propagate higher up in the atmosphere as evident from the differences between the phase difference spectra of the non-magnetic and the magnetic model. We explore different causes that may lead to the observed signatures and the differences in the phase difference spectra of the waves. We conclude that the internal waves in the quiet Sun most likely undergo mode coupling to the slow magneto-acoustic waves as described by [Newington & Cally \(2010, 2011\)](#) and are mostly reflected back into the atmosphere. Looking at the height dependence of the phase spectra, we confirm that this reflection happens well within the region where the average plasma- β is larger than 1 (i.e. within the gas-dominated region), confirming the mode-coupling scenario. This is also in agreement with the energy flux spectra, which shows a mixed upward and downward transport of energy in the internal gravity wave regime for the magnetic case in the higher layers. Since the magnetic fields in our model are mostly vertical, conversion to Alfvén waves is highly unlikely. Conversion to Alfvén waves is not facilitated unless there is a significantly inclined magnetic field present. The effect of the horizontal fields on the propagation of internal waves will be explored in a later paper. We also note out that the strong suppression that is observed within magnetic flux-concentration ([Straus et al. 2008](#)) may be the effect of non-linear wave breaking due to the vortex flows that are ubiquitously present in these regions. We also find that the surface-gravity waves are strongly suppressed in the magnetic model as we go higher up in the atmosphere, likely due to the strong vertical component of the magnetic field.

The analysis presented in this paper is based on models computed with different numerical solvers, which resulted in a smaller size of the granules in the non-magnetic run. However, a preliminary study using the identical MHD solver for both runs shows that the par-

ticular propagation properties of internal waves that are found in this paper are independent of the solver. The granules are of the same size and match with the sizes that we see in the magnetic model of the present paper.

This analysis has shown that the internal waves are strongly affected by the magnetic fields present on the Sun. Recognizing that a considerable amount of internal wave flux is produced in the near surface layers, and that these waves can couple with other magneto-atmospheric waves, it is important to fully understand the transfer of energy from these waves to other waves in the atmosphere of the Sun. In a broader context, a clear insight into the internal wave spectrum will help us to connect the missing link in our understanding of all the different wave phenomena in the solar atmosphere and their individual role in heating the upper atmosphere either directly or indirectly.

This work was supported by a NASA EPSCoR award to NMSU under contract No. NNX09AP76A and NSF PAARE award AST-084 9986. The research leading to these results has received funding from the European Research Council under the European Union’s Seventh Framework Programme (FP7/2007-2013) / ERC Grant Agreement n.307117 and n.312844. We especially thank Stuart Jefferies for his talk at the Fifty Years of Seismology of the Sun and Stars conference in Tucson, that stimulated our interest in studying internal gravity waves. The authors are grateful to Bernhard Fleck for detailed comments on a draft of this paper. GV acknowledges the helpful discussions with Markus Roth, Nazaret Bello González, Patrick Gaulme, Thierry Apourchoux, and the CO⁵BOLD community. We would like to thank the anonymous referee for his/her detailed comments, which helped us to improve the paper.

Software: CO⁵BOLD ([Freytag et al. 2012](#))

REFERENCES

- Artru, J., Ducic, V., Kanamori, H., Lognonné, P., & Murakami, M. 2005, *GeoJI*, 160, 840, [[2005GeoJI.160..840A](#)]
- Bogdan, T. J., & Cally, P. S. 1997, *RSPSA*, 453, 943, [[1997RSPSA.453..943B](#)]
- Bonet, J. A., Marquez, I., Vazquez, M., & Woehl, H. 1991, *A&A*, 244, 492, [[1991A&A...244..492B](#)]
- Cally, P. S. 2001, *ApJ*, 548, 473, [[2001ApJ...548..473C](#)]
- Campos, L. M. B. C., & Marta, A. C. 2015, *GApFD*, 109, 168, [[2015GApFD.109..168C](#)]
- Clark, P. A., & Clark, Jr., A. 1973, *SoPh*, 30, 319, [[1973SoPh...30..319C](#)]
- Cram, L. E. 1978, *A&A*, 70, 345, [[1978A&A...70..345C](#)]
- Deubner, F.-L., & Fleck, B. 1989, *A&A*, 213, 423, [[1989A&A...213..423D](#)]
- . 1990, *A&A*, 228, 506, [[1990A&A...228..506D](#)]
- Deubner, F.-L., Fleck, B., Marmolino, C., & Severino, G. 1990, *A&A*, 236, 509, [[1990A&A...236..509D](#)]
- Deubner, F.-L., Fleck, B., Schmitz, F., & Straus, T. 1992, *A&A*, 266, 560, [[1992A&A...266..560D](#)]
- Deubner, F.-L., & Gough, D. 1984, *ARA&A*, 22, 593, [[1984ARA&A...22..593D](#)]
- Durrant, C. J., & Nesis, A. 1981, *A&A*, 95, 221, [[1981A&A...95..221D](#)]
- Ferraro, C. A., & Plumpton, C. 1958, *ApJ*, 127, 459, [[1958ApJ...127..459F](#)]
- Fleck, B., & Deubner, F.-L. 1989, *A&A*, 224, 245, [[1989A&A...224..245F](#)]
- Frazier, E. N. 1968, *ApJ*, 152, 557, [[1968ApJ...152..557F](#)]
- Freytag, B., Steffen, M., Ludwig, H.-G., et al. 2012, *JCoPh*, 231, 919, [[2012JCoPh.231..919F](#)]

- Gustafsson, B., Edvardsson, B., Eriksson, K., et al. 2008, *A&A*, 486, 951, [2008A&A...486..951G]
- Hasan, S. S., & Christensen-Dalsgaard, J. 1992, *ApJ*, 396, 311, [1992ApJ...396..311H]
- Hasan, S. S., & Kalkofen, W. 1999, *ApJ*, 519, 899, [1999ApJ...519..899H]
- Hayashi, Y. 1982, *J. Meteor. Soc. Japan Ser. II*, 60, 156
- Hines, C. O. 1960, *CaJPh*, 38, 1441, [1960CaJPh..38.1441H]
- Kato, Y., Steiner, O., Steffen, M., & Suematsu, Y. 2011, *ApJL*, 730, L24, [2011ApJ...730L..24K]
- Khomenko, E., & Cally, P. S. 2012, *ApJ*, 746, 68, [2012ApJ...746...68K]
- Kneer, F., & Bello González, N. 2011, *A&A*, 532, A111, [2011A&A...532A.111K]
- Kneer, F., & von Uexküll, M. 1993, *A&A*, 274, 584, [1993A&A...274..584K]
- Komm, R., Mattig, W., & Nesis, A. 1991, *A&A*, 252, 827, [1991A&A...252..827K]
- Krijger, J. M., Rutten, R. J., Lites, B. W., et al. 2001, *A&A*, 379, 1052, [2001A&A...379.1052K]
- Kuperus, M. 1969, *SSRv*, 9, 713, [1969SSRv....9..713K]
- Leibacher, J. W., & Stein, R. F. 1971, *Astrophys. Lett.*, 7, 191, [1971ApL.....7..191L]
- . 1981, *NASSP*, 450, 263, [1981NASSP.450..263L]
- Leighton, R. B. 1960, in *IAU Symposium*, Vol. 12, *Aerodynamic Phenomena in Stellar Atmospheres*, ed. R. N. Thomas, 321–325, [1960IAUS...12..321L]
- Leighton, R. B., Noyes, R. W., & Simon, G. W. 1962, *ApJ*, 135, 474, [1962ApJ...135..474L]
- Leroy, B., & Schwartz, S. J. 1982, *A&A*, 112, 84, [1982A&A...112...84L]
- Lighthill, J. 2001, *Waves in Fluids* (Cambridge University Press), [2001wafL.book.....L]
- Lighthill, M. J. 1967, in *IAU Symposium*, Vol. 28, *Aerodynamic Phenomena in Stellar Atmospheres*, ed. R. N. Thomas, 429, [1967IAUS...28..429L]
- Lindzen, R. S. 1988, *PAPGe*, 126, 103, [1988PAPGe.126..103L]
- Lites, B. W., & Chipman, E. G. 1979, *ApJ*, 231, 570, [1979ApJ...231..570L]
- Lites, B. W., Kubo, M., Socas-Navarro, H., et al. 2008, *ApJ*, 672, 1237, [2008ApJ...672.1237L]
- Logan, J. D., & Hill, H. A. 1980, *SSRv*, 27, 301, [1980SSRv...27..301L]
- Marmolino, C., & Severino, G. 1991, *A&A*, 242, 271, [1991A&A...242..271M]
- Mihalas, B. W., & Toomre, J. 1981, *ApJ*, 249, 349, [1981ApJ...249..349M]
- . 1982, *ApJ*, 263, 386, [1982ApJ...263..386M]
- Moore, D. W., & Spiegel, E. A. 1964, *ApJ*, 139, 48, [1964ApJ...139...48M]
- Mosser, B. 1995, *A&A*, 293, [1995A&A...293..586M]
- Nagashima, K., Löptien, B., Gizon, L., et al. 2014, *SoPh*, 289, 3457, [2014SoPh..289.3457N]
- Newington, M. E., & Cally, P. S. 2010, *MNRAS*, 402, 386, [2010MNRAS.402..386N]
- . 2011, *MNRAS*, 417, 1162, [2011MNRAS.417.1162N]
- Orozco Suárez, D., & Bellot Rubio, L. R. 2012, *ApJ*, 751, 2, [2012ApJ...751....2O]
- Priest, E. 2014, *Magnetohydrodynamics of the Sun* (Cambridge University Press), [ISBN: 9780521854719]
- Rutten, R. J., & Krijger, J. M. 2003, *A&A*, 407, 735, [2003A&A...407..735R]
- Sangeetha, C. R., & Rajaguru, S. P. 2016, *ApJ*, 824, 120, [2016ApJ...824..120S]
- Schatzman, E., & Souffrin, P. 1967, *ARA&A*, 5, 67, [1967ARA&A...5...67S]
- Schmieder, B. 1976, *SoPh*, 47, 435, [1976SoPh...47..435S]
- Schmitz, F., & Fleck, B. 1998, *A&A*, 337, 487, [1998A&A...337..487S]
- Shelyag, S., Keys, P., Mathioudakis, M., & Keenan, F. P. 2011, *A&A*, 526, A5, [2011A&A...526A...5S]
- Spiegel, E. A. 1957, *ApJ*, 126, 202, [1957ApJ...126..202S]
- Staiger, J. 1987, *A&A*, 175, 263, [1987A&A...175..263S]
- Staiger, J., Mattig, W., Schmieder, B., & Deubner, F.-L. 1984, *Mem. Soc. Astron. Italiana*, 55, 147, [1984MmSAI..55..147S]
- Steiner, R. F. 1967, *SoPh*, 2, 385, [1967SoPh....2..385S]
- Steiner, O., Rajaguru, S. P., Vigeesh, G., et al. 2013, *MSAIS*, 24, 100, [2013MSAIS..24..100S]
- Steiner, O., & Rezaei, R. 2012, in *Astronomical Society of the Pacific Conference Series*, Vol. 456, *Fifth Hinode Science Meeting*, ed. L. Golub, I. De Moortel, & T. Shimizu, 3, [2012ASPC..456....3S]
- Stix, M. 1970, *A&A*, 4, 189, [1970A&A....4..189S]
- Stodilka, M. I. 2008, *MNRAS*, 390, L83, [2008MNRAS.390L..83S]
- Straus, T., & Bonaccini, D. 1997, *A&A*, 324, 704, [1997A&A...324..704S]
- Straus, T., Fleck, B., Jefferies, S. M., et al. 2008, *ApJL*, 681, L125, [2008ApJ...681L.125S]
- Sutherland, B. R. 2010, *Internal Gravity Waves* (Cambridge University Press), [ISBN: 9780521839150]
- Thomas, J. H., Clark, P. A., & Clark, Jr., A. 1971, *SoPh*, 16, 51, [1971SoPh...16...51T]
- Uchida, Y. 1965, *ApJ*, 142, 335, [1965ApJ...142..335U]
- . 1967, *ApJ*, 147, 181, [1967ApJ...147..181U]
- Ulrich, R. K. 1970, *ApJ*, 162, 993, [1970ApJ...162..993U]
- Vigeesh, G., Hasan, S. S., & Steiner, O. 2009, *A&A*, 508, 951, [2009A&A...508..951V]
- Wedemeyer-Böhm, S., Scullion, E., Steiner, O., et al. 2012, *Nature*, 486, 505, [2012Natur.486..505W]
- Whitaker, W. A. 1963, *ApJ*, 137, 914, [1963ApJ...137..914W]
- Zhugzhda, I. D., & Dzhililov, N. S. 1982, *A&A*, 112, 16, [1982A&A...112...16Z]
- . 1984, *A&A*, 132, 45, [1984A&A...132...45Z]